ARTICLES
https://doi.org/10.1038/s41565-017-0022-x
nature nanotechnology

# Strain distributions and their influence on electronic structures of $WSe_2$–$MoS_2$ laterally strained heterojunctions

Chendong Zhang[1,2*], Ming-Yang Li[3,4], Jerry Tersoff[5], Yimo Han[6], Yushan Su[1,7], Lain-Jong Li[3], David A. Muller[6,8] and Chih-Kang Shih[1*]

**Monolayer transition metal dichalcogenide heterojunctions, including vertical and lateral p–n junctions, have attracted considerable attention due to their potential applications in electronics and optoelectronics. Lattice-misfit strain in atomically abrupt lateral heterojunctions, such as $WSe_2$–$MoS_2$, offers a new band-engineering strategy for tailoring their electronic properties. However, this approach requires an understanding of the strain distribution and its effect on band alignment. Here, we study a $WSe_2$–$MoS_2$ lateral heterojunction using scanning tunnelling microscopy and image its moiré pattern to map the full two-dimensional strain tensor with high spatial resolution. Using scanning tunnelling spectroscopy, we measure both the strain and the band alignment of the $WSe_2$–$MoS_2$ lateral heterojunction. We find that the misfit strain induces type II to type I band alignment transformation. Scanning transmission electron microscopy reveals the dislocations at the interface that partially relieve the strain. Finally, we observe a distinctive electronic structure at the interface due to hetero-bonding.**

Semiconductor heterojunctions are essential building blocks for future electronics and photonics. In particular, the emergence of two-dimensional (2D) semiconducting materials such as transition metal dichalcogenides (TMDs) could lead to the realization of next-generation ultrathin devices[1–5]. Apart from vertically stacked van der Waals heterostructures[6–10], monolayer lateral heterojunctions with a line interface between two dissimilar TMDs have been successfully demonstrated[11–14]. Notably, lattice-mismatched in-plane heterojunctions such as $WSe_2$–$MoS_2$[14] introduce the intriguing possibility of producing novel electronic structures via strain engineering. Additionally, the electronic structures of TMDs can be substantially influenced by strain[15–19]. However, determination of the strain is usually indirect[20–23], yielding inconsistent results for the quantitative dependence of the bandgap on strain. Moreover, the experimental techniques used to determine the strain and bandgaps are mostly optical techniques such as Raman spectroscopy and photoluminescence spectroscopy, which are diffraction limited with a maximum resolution of 500 nm[22–26]. In this work, we map the anisotropic strain tensor with nanometre resolution and reveal its influence on the electronic structure. $WSe_2$–$MoS_2$ lateral heterojunctions are grown using chemical vapour deposition following procedures similar to those described earlier[14] (see Methods). Instead of insulating sapphire substrates, here, highly oriented pyrolytic graphite (HOPG) is used to enable scanning tunnelling microscopy (STM) investigations. Figure 1a shows a typical STM image of a triangular $WSe_2$ core surrounded by $MoS_2$. These triangular $WSe_2$ cores commonly have an edge length between 200 and 400 nm, and the surrounding $MoS_2$ has a typical width of 100–200 nm. On closer examination (Fig. 1b), we find that the interface is composed of short straight sections (5–15 nm) separated by kinks that appear as bright spots due to adsorbates at these sites. In addition, some segments are not straight. This result is consistent with previously reported transmission electron microscopy observations[14] showing that the interface mostly consists of straight zigzag segments, whereas some segments contain mixed zigzag and armchair sections, creating locally meandering segments. The apparent topographical height difference between the $WSe_2$ and $MoS_2$ regions is ~1 Å, which is the same as the height difference measured from isolated monolayer $WSe_2$ and $MoS_2$ on graphite (Supplementary Section 1). The abrupt change in topographical contrast implies a chemically abrupt transition across the interface, as was seen in previous studies of similar samples grown on a sapphire substrate[14].

A close-up view across a straight segment of the interface (Fig. 1c) shows a hexagonal moiré pattern due to the lattice mismatch of the monolayer TMD on graphite. The periodicity of ~1 nm observed here indicates a nearly zero rotation angle between the TMD and the graphite substrate (Supplementary Section 2). This straight interface segment is confirmed to be along the zigzag direction of the atomic lattices. Previous transmission electron microscopy investigations have shown that the triangular $WSe_2$ core has W atoms at the terminals, and the subsequent $MoS_2$ growth leads to the formation of a '$WS_2$-like' line interface[14] as schematically illustrated in Fig. 1d. Considering that $MoS_2$ and $WSe_2$ have a lattice mismatch of 3.8% (3.282 Å for $WSe_2$ and 3.160 Å for $MoS_2$), a seamless interface should lead to significant strain. Moreover, such strain should be inherently anisotropic. Careful calibrations of atomic images have enabled the measurement of the strain in systems such as $In_{0.5}Ga_{0.5}As$ quantum dots in GaAs[27]. Nevertheless, it is challenging to achieve a precision better than 2–3%. As discussed recently, the moiré pattern can be used as a 'magnifying glass' for

[1]Department of Physics, University of Texas at Austin, Austin, TX, USA. [2]School of Physics and Technology, Wuhan University, Wuhan, China. [3]Physical Sciences and Engineering Division, King Abdullah University of Science and Technology, Thuwal, Saudi Arabia. [4]Research Center for Applied Sciences, Academia Sinica, Taipei, Taiwan. [5]IBM Research Division, T. J. Watson Research Center, Yorktown Heights, NY, USA. [6]School of Applied and Engineering Physics, Cornell University, Ithaca, NY, USA. [7]School of the Gifted Young, University of Science and Technology of China, Hefei, Anhui, China. [8]Kavli Institute at Cornell for Nanoscale Science, Cornell University, Ithaca, NY, USA. *e-mail: cdzhang@whu.edu.cn; shih@physics.utexas.edu

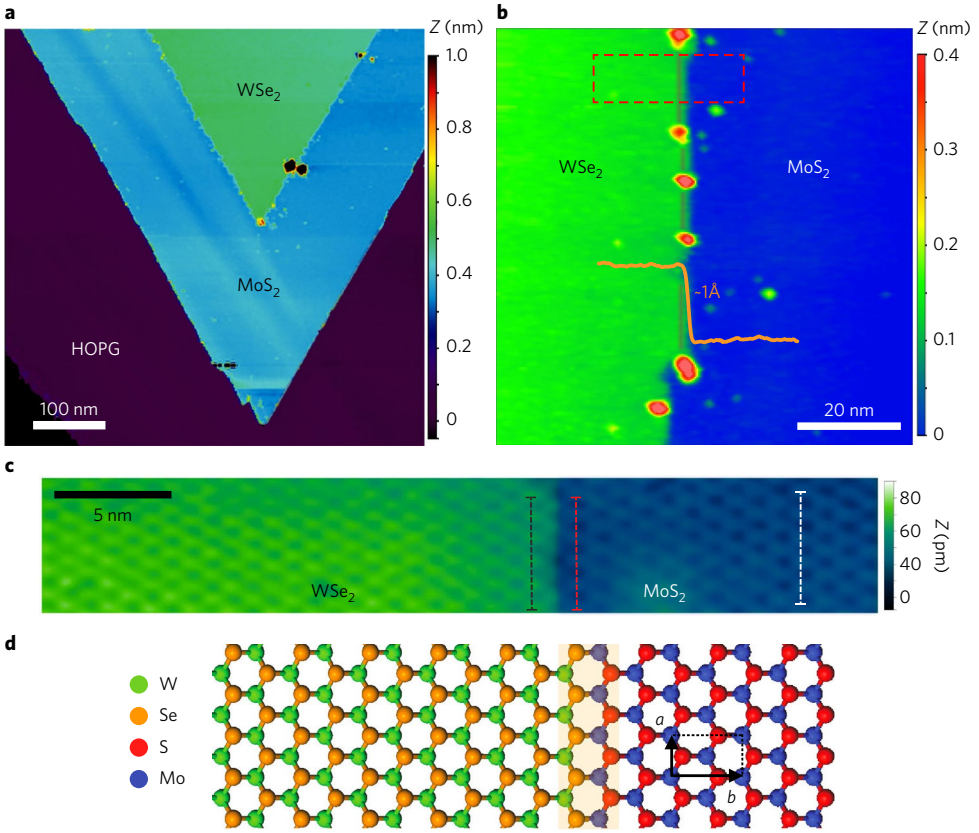


**Fig. 1 | STM images of the $WSe_2$–$MoS_2$ lateral heterojunction. a**, Large-scale STM image showing that the inner $WSe_2$ core is surrounded by a $MoS_2$ skirt. **b**, Close-up image of the interface showing that the straight segments are separated by kinks. The height profile indicates the thickness difference between $WSe_2$ and $MoS_2$. **c**, Zoomed-in image of a straight interface segment (the dashed rectangle in **b**). The moiré pattern formed with the graphite shows a period of ~1 nm. Three marks with identical length are labelled along the zigzag direction. The two marks near the interface (in black and red) span across five lattice spacings, whereas the white mark fails to span the same number of lattice spacings. **d**, Model of the $WSe_2$–$MoS_2$ heterojunction with a W–S line interface. Strain in the $MoS_2$ region is not displayed. The centred rectangular lattice is labelled with black dashed lines. ***a*** and ***b*** represent the vectors along the zigzag and armchair directions, respectively. Scanning parameters: **a**, 3 V, 4 pA; **b**, 3 V, 5 pA; **c**, −1 V, 25 pA.

observing changes in lattice constants[28,29]. The magnification factor is deduced in Supplementary Section 2 as the reciprocal of the lattice mismatch. The relatively large lattice mismatch (>30%) between the graphite and the TMD leads to a small magnification factor of approximately three. Therefore, it is difficult to directly visualize the strain (for details, see Supplementary Section 3). However, with careful calibration, one can conclude that in the $MoS_2$ region, starting from the interface and moving into the $MoS_2$ interior by 7.5 nm, the moiré pattern periodicity along the zigzag direction changes by ~7 ± 2%. This result implies a change in atomic lattice constant along the zigzag direction by ~2.2 ± 0.5%. This point will be elaborated further below.

## Mapping the two-dimensional strain tensor

The situation changes dramatically when such a lateral $WSe_2$–$MoS_2$ heterostructure is grown on top of an underlying $WSe_2$ monolayer, as shown by the STM image in Fig. 2a. No moiré pattern is observed in the second layer $WSe_2$ core region, implying a rotational alignment with the underlying $WSe_2$. In the $MoS_2$ region, a moiré pattern with serious distortion is observed clearly. This effect is due to a much higher magnification factor (>20) of the moiré pattern resulting from a small lattice mismatch between the underlying $WSe_2$ monolayer and the strained $MoS_2$.

The existence of lines of the moiré pattern running parallel to the interfacial zigzag direction indicates that in the strained $MoS_2$, the atomic zigzag lattice lines are still well aligned along the zigzag interface. To analyse the strain, we choose a centred rectangular lattice with lattice vectors **a** and **b** as labelled in Fig. 1d, where **a** is along the zigzag direction parallel to the interface and **b** is along the perpendicular direction (namely, the armchair direction). For unstrained, rotationally aligned $MoS_2$ on $WSe_2$, the moiré pattern is also a rotationally aligned regular hexagonal superlattice with a lattice constant $\lambda_a$ of 8.6 nm (Supplementary Section 2). The corresponding $\lambda_b$ would be $\sqrt{3}\,\lambda_a = 15.0$ nm.

This value is indeed observed in a strain-free $MoS_2$ flake stacked on $WSe_2$ (left panel of Fig. 2b). In the lateral $MoS_2$–$WSe_2$ heterojunction, the epitaxial growth of $MoS_2$ along the zigzag interface naturally leads to a tensile strain along **a**, presumably accompanied by a compressive strain along the **b** direction. Moreover, one can see an obvious shear strain in the moiré lattices due to the existence of a strain gradient in the atomic lattice. Note that in the moiré patterns, the shear angle is also greatly amplified with respect to the atomic lattice shear angle. Below, we show that by carefully analysing the geometry of moiré patterns, one can fully determine the local 2D strain tensor in the $MoS_2$ atomic lattice.

Due to the presence of shear strain and a strain gradient, the moiré pattern should be characterized as a centred trapezoid instead of a centred rectangle, as shown in Fig. 2b. As discussed in Supplementary Section 2, moiré pattern spacings $\lambda_a$ and $\lambda_b$ along the a***a*** and b***b*** directions (Fig. 2b) can be expressed as follows:

$$\lambda_a = a'_{\mathrm{Mo}} / \delta_a, \text{ with } \delta_a = |\, a_{\mathrm{W}} - a'_{\mathrm{Mo}} \,| / a_W \qquad (1)$$

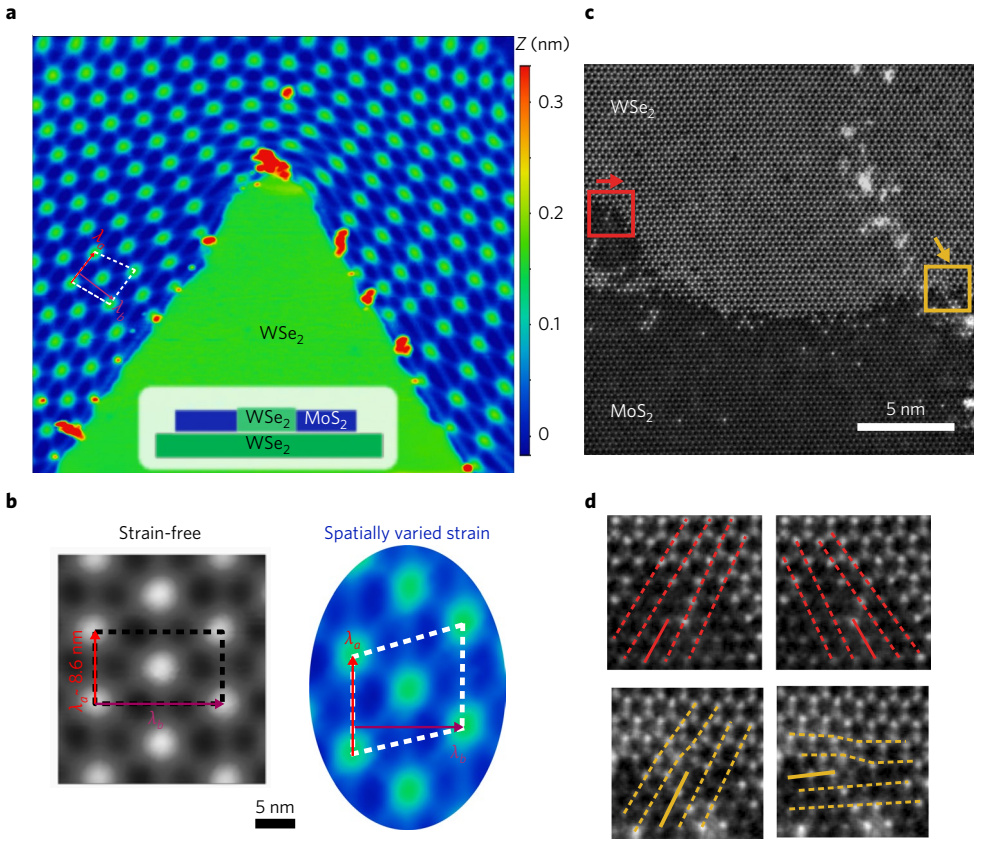


**Fig. 2 | Imaging the anisotropic strain in the $WSe_2$–$MoS_2$ lateral heterojunction. a**, STM image of a lateral $WSe_2$–$MoS_2$ heterojunction stacked on top of a monolayer $WSe_2$. The inset schematically illustrates the stacking conformation. **b**, The left panel shows an example of the moiré pattern on an $MoS_2$/$WSe_2$ stack where both layers are strain-free. The right panel shows a close-up image of the moiré pattern in **a**. A centred rectangle and trapezoid are marked by dashed lines for the strain-free and strained cases, respectively. The periodicities $\lambda_a$ and $\lambda_b$ are labelled correspondingly. **c**, Atomically resolved ADF-STEM image of a lateral heterojunction with two misfit dislocations sectioned off. The orientations of two different Burger's vectors are indicated by arrows in red (0° to the interface) and yellow (60° to the interface), respectively. **d**, Magnified images with labelled atomic planes (dashed lines) along the [1000] (left column) and the [0100] (right column) directions. The extra atomic planes that create the misfits are indicated by solid lines. The upper and lower panels correspond to the 0° and 60° Burger's vectors, respectively. Scanning parameters: **a**, 3 V, 5 pA.

$$\lambda_b = b'_{\mathrm{Mo}} / \delta_b, \text{ with } \delta_b = | b_{\mathrm{W}} - b'_{\mathrm{Mo}} | / b_{\mathrm{W}} \quad (2)$$

Here, $a_w$ and $b_w$ are the lattice constants for a centred rectangular lattice in $WSe_2$ (unstrained) along the two principal axes, and $a'_{Mo}$ and $b'_{Mo}$ are the lattice constants for strained $MoS_2$. $\delta_a$ and $\delta_b$ are the lattice mismatches. These two expressions show that the moiré pattern spacing, which is related to the atomic lattice constant, is amplified by a factor that is inversely proportional to the mismatch. Therefore, a tensile strain in $MoS_2$ will reduce the mismatch, thus enlarging the moiré pattern periodicity; conversely, compressive strain will reduce the moiré pattern periodicity.

Similarly, the shear angle of moiré pattern $\beta$ is amplified with respect to the atomic lattice shear angle $\alpha$ by a factor $A_\beta$,

$$tan\beta = A_\beta tan\alpha, \text{ with } A_\beta = \frac{1}{\delta_a} \quad (3)$$

The angular amplification factor $A_\beta = 1/\delta_a$ is the same as the moiré periodicity amplification factor along **a** because the atomic shear angle is related to the displacement along **a** related to the rotation of **b** axis. Thus, from the analysis of the moiré lattice, one can determine the 2D strain tensor

$$\begin{bmatrix} \varepsilon_{aa} & \varepsilon_{ab} \\ \varepsilon_{ba} & \varepsilon_{bb} \end{bmatrix}$$

The measurement of $\lambda_a$ enables us to determine $1/\delta_a$, from which the strain along **a**, $\varepsilon_{aa}$ can be determined. Similarly, the measurement of $\lambda_b$ determines $\varepsilon_{bb}$, and $\beta$ determines $\varepsilon_{ab}$ and $\varepsilon_{ba}$. The detailed derivation is provided in Supplementary Section 2. Note that a tensile strain will lead to a smaller $\delta_a$ and thus a larger amplification factor for $\lambda_a$ (that is, elongated moiré lattice spacing), whereas a compressive strain along **b** (negative $\varepsilon_{bb}$) will lead to a smaller amplification factor for $\lambda_b$ (that is, compressed moiré spacing along **b**). Using the experimental moiré pattern shown in the right panel of Fig. 2b as an example, the strain tensor at the centre lattice point is determined as $\varepsilon_{aa} = 1.17\%$, $\varepsilon_{bb} = -0.26\%$ and $\varepsilon_{ab} = \varepsilon_{ba} = 0.69\%$. Note that a shear strain of 0.69% corresponds to a shear angle of only 0.4°. Such a minor distortion in the atomic lattice can now be observed prominently using the magnifying glass of moiré patterns. Note that the moiré pattern actually measures the difference in strain between the surface and subsurface layers; thus, the accuracy of this quantitative determination relies on the assumption that the underlying $WSe_2$ retains its original lattice constant. No strain was observed in previous studies of the van der Waals stacking of flakes of different TMDs[6, 30]; therefore, this approximation should be reasonable. However, we cannot rule out that some of the resulting strain could be transferred to the substrate once the heterostructure forms.

In Fig. 3e,f, the experimental result for $\varepsilon_{aa}$ and $\varepsilon_{bb}$ is plotted as a function of distance from the interface. Note that $\varepsilon_{aa}$ data are not

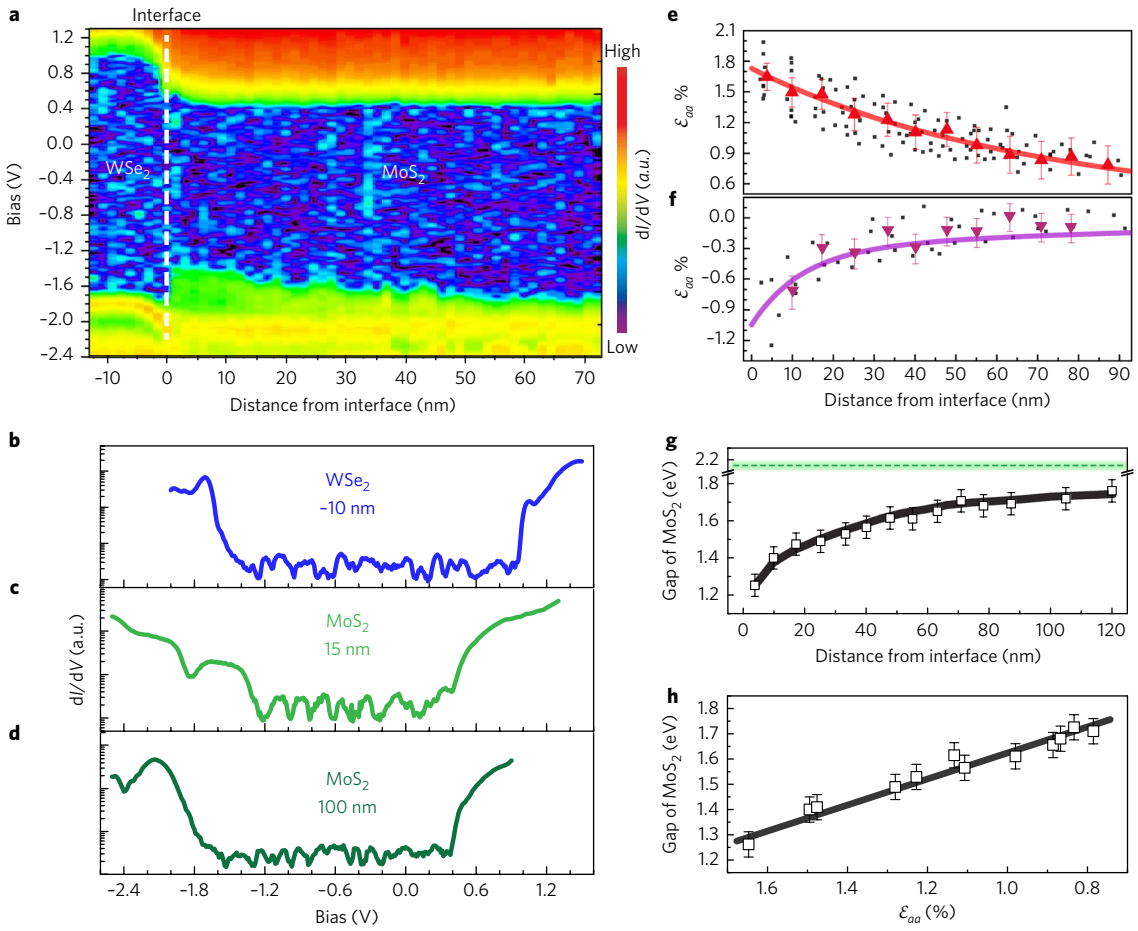


**Fig. 3 | The electronic structure and its dependence on the strain distribution. a**, A band profile map plotted in terms of Log(d*I*/d*V*) (shown by the colour scale). The location of the interface at 0 nm is marked by a dashed line, and the $WSe_2$ and $MoS_2$ regions are labelled. **b**–**d**, Typical d*I*/d*V* spectra for $WSe_2$ (**b**) and $MoS_2$ (**c**,**d**) with the distance from the interface labelled. The stabilized bias and set-point current are as follows: **a**, −2.4 V, 25 pA; **b**, −1.9 V, 25 pA; **c** and **d**, −2.5 V, 25 pA. **e**, **f**, The decays of strain tensors $\varepsilon_{aa}$ (**e**) and $\varepsilon_{bb}$ (**f**) with the distance from the interface. The black dots represent experimental results for each of the super lattice spots measured at multiple regions around the same $WSe_2$ core. The triangular markers in **e** and **f** are the averaged values of each zigzag moiré lattice line in a representative region (shown in Supplementary Fig. S4b). The solid curve in **e** is a fit to the triangles using $\varepsilon_{aa} = A(x+L)^{-2}$, analogous to a circular inclusion in an infinite sheet[31] where $L = 170$ nm is the diameter of the $WSe_2$ core and $A$ is a proportionality factor. **g**, The quasiparticle bandgaps as a function of the distance from the interface. The green dashed line at 2.15 eV indicates the gap of the strain-free $MoS_2$[34]. The solid curve is a fit to guide the eye. **h**, The dependence of quasiparticle bandgaps on $\varepsilon_{aa}$. A linear fitting with a slope of 0.52 eV per 1% $\varepsilon_{aa}$ strain is drawn in black. The triangles in **e** and the data points in **g** are used to generate **h**. The error bars in **e**–**h** are based on statistics of multiple measurements.

available until 3.5 nm away from the interface where the first moiré lattice line starts (and ~5 nm for $\varepsilon_{bb}$). The overall trend shows systematic decay of both $\varepsilon_{aa}$ and $\varepsilon_{bb}$ as one moves away from the interface, with the decay of $\varepsilon_{bb}$ being unexpectedly rapid. For example, at 50 nm away from the interface, $\varepsilon_{bb}$ drops from −0.9% to −0.2%, more than a factor of 4, whereas $\varepsilon_{aa}$ drops by less than a factor of 2, from 1.7% to 1.0%.

When extrapolated to the interface, the tensile strain $\varepsilon_{aa}$ is 1.76%, much less than the mismatch of 3.8%; this result can only be explained by the presence of a significant density of dislocations at the interface. The average distance between the adsorbate/kink sites (as shown in Fig. 1a) is ~14 ± 3 nm (Supplementary Section 4). If we interpret these sites as the locations of misfit dislocation, then with a Burger's vector of 0.32 nm, we would expect such dislocations to provide a partial strain relaxation of 2.3 ± 0.5% at the interface. This value is consistent with the experimental results presented above. Indeed, we have confirmed the presence of such misfit dislocations using annular dark-field scanning transmission electron microscopy (ADF-STEM). We actually find two types of dislocations: the majority are pure misfit dislocations, with the Burger's vector along the zigzag direction parallel to the interface (upper panel in Fig. 2d). However, some dislocations, while also along the zigzag direction, are at 60° to the interface (lower panel in Fig. 2d). The ADF-STEM experiments are carried out on $MoS_2$–$WSe_2$ lateral heterojunctions grown on sapphire substrates, which differ in domain size (for details see Supplementary Section 4).

We next discuss the contrasting decay behaviour of $\varepsilon_{aa}$ versus $\varepsilon_{bb}$. The strain around an inclusion in an infinite sheet is expected to decay gradually with distance[31]. We see this behaviour for $\varepsilon_{aa}$. However, for $\varepsilon_{bb}$ we see a much more rapid decay, probably because there is a free edge during growth, which can allow relaxation of stress normal to the interface. If the stress is fully relaxed in the normal direction, then the strain should be given by $\varepsilon_{bb} = -\nu\varepsilon_{aa}$, where $\nu$ is the Poisson ratio. More generally, we expect a form such as $\varepsilon_{bb} = C\sigma_{bb} - \nu\varepsilon_{aa}$, where $C$ is a compliance and $\sigma$ is the stress. If we assume a simple exponential decay of the compressive stress $\sigma_{bb}$ with distance from the interface due to some progressive relaxation mechanism, we can fit the strain with $C\sigma_{bb} = -0.65 \times e^{-d/12nm}$ and $\nu = 0.2$, close to the value $\nu = 0.25$ predicted for unsupported $MoS_2$ monolayers[32,33].

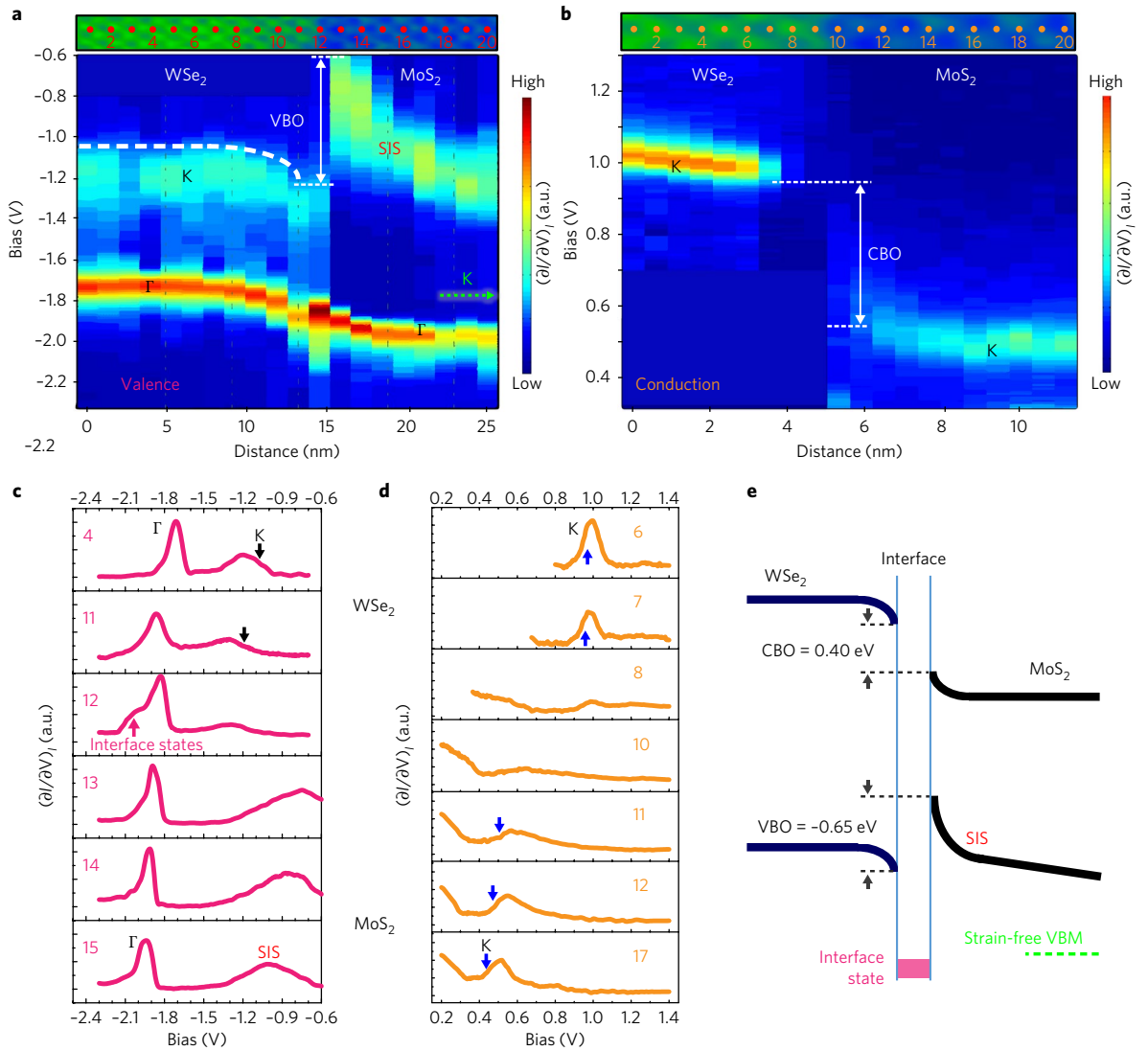


**Fig. 4 | Determinations of band edges, interface states and band alignment by constant *I* spectroscopy. a**,**b**, Colour-coded rendering of $(\partial I/\partial V)_I$ mappings for the valence band and conduction band, respectively. The spectra numbers and their locations (red spots) are labelled in the corresponding topography images. The step sizes in **a** and **b** are 0.6 nm and 1.3 nm, respectively. The VBO, CBO and the SIS are clearly seen. The green arrow in **a** represents the estimated energy location of the K point in strain-free $MoS_2$. **c**, Selective subset of $(\partial I/\partial V)_I$ spectra for the valence band. Spectrum 12 shows the interface state at −2.0 eV. The black arrows in spectra 4 and 11 indicate the energy locations of the K point. The SIS can be seen as a peak in spectra 13–15. **d**, Selective subset of $(\partial I/\partial V)_I$ spectra for the conduction band. The blue arrows indicate the shifting of the CBM (at the K point) for $WSe_2$ and $MoS_2$. The stabilized bias and set-point current are as follows: **a**, −2.3 V, 25 pA; **b**, 1.3 V, 20 pA. **e**, Type I band alignments between $WSe_2$ and $MoS_2$, with the CBO and VBO labelled.

## The effect of strain on the electronic structures

The influence of strain on the electronic structures is investigated using scanning tunnelling spectroscopy (STS). Figure 3a shows the d$I$/d$V$ (where $I$ is the tunnelling current and $V$ is the bias voltage) mapping across 84 nm for monolayer $MoS_2$–$WSe_2$ on graphite. The $WSe_2$ region exhibits classic band bending, with the valence and conduction edges bending downward and parallel at the interface. We see a sharp transition at the interface, with a smaller bandgap in the $MoS_2$ region, and a slight upward bending of the $MoS_2$ conduction band at the interface. However, the $MoS_2$ valence band shows an unexpected strong spatial variation of the electronic structure. We determine that this effect is due to the strain field present in the $MoS_2$ region. Representative d$I$/d$V$ spectra taken at different distances from the interface are shown in Fig. 3b–d. Clear deviation from the typical $MoS_2$ electronic structures is seen in the strained region (Fig. 3c). For monolayer TMDs, it has been shown that d$I$/d$V$ measured at a constant tip-to-sample separation $Z$ has a limited dynamic range for capturing fine structures near the band edge due to the influence of the parallel momentum in the tunnelling decay constant $\kappa$[34]. Instead, a constant current spectroscopy method is adopted following a previously described method[34] to more accurately determine the bandgap (Supplementary Section 5). The resulting bandgap in $MoS_2$ as a function of distance from the interface is plotted in Fig. 3g. The bandgap variation in $MoS_2$, albeit measured for heterojunctions on graphite, also shows a long decay length of ~100 nm, similar to that of $\varepsilon_{aa}$ measured for $WSe_2$–$MoS_2$ on $WSe_2$. This result supports our conjecture that the strain distribution for heterojunctions on $WSe_2$ or on graphite are similar. This result further allows us to determine the strain dependence of the bandgap reduction in $MoS_2$ (Fig. 3h), from which a value of ~0.5 eV bandgap reduction per 1% $\varepsilon_{aa}$ strain is deduced.

The electronic structure is mapped across the interface at a finer spatial resolution in Fig. 4a,b, which shows constant current tunnelling spectroscopy $(\partial I/\partial V)_I$ for the valence band and the conduction band, respectively. Individual spectra taken along the path across the interface are labelled in the accompanying STM image above. Selected individual spectra are displayed in Fig. 4c,d, respectively for the valence band and the conduction band, and the numbers on the spectra refer to their positions in the complete set as labelled. In the $WSe_2$ region, spectrum 4 is essentially the same as those acquired on isolated $WSe_2$ on graphite with the Γ point at $-1.70 \pm 0.03$ eV and the K point located at $-1.05 \pm 0.03$ eV (that is, 0.65 eV above the Γ point). Moving towards the interface, the $WSe_2$ spectra are identical except for the band bending downward by ~0.15 eV within the last 5 nm from the interface. In the $MoS_2$ region near the interface, the systematic upward band bending can also be observed for the Γ states. However, unlike the isolated $MoS_2$ on graphite where the valence band minimum (VBM) is located at ~0.2 eV above the Γ point, here, we observe a state with a large separation from the Γ states. Moreover, the closer we move towards the interface (that is, the larger the strain), the larger the separation. We attribute this feature to strain-induced states (SISs). Interestingly, these SISs show a large $\kappa$ value in the decay constant measurement (Supplementary Section 6), suggesting that they are located at the corner of the distorted Brillouin zone=, similar to the K point of the undistorted situation. The appearance of this SIS in the valence band is responsible for the reduction of the bandgap, the magnitude of which correlates well with the strain (Fig. 3e and Supplementary Fig. S10c). Immediately at the interface, an intriguing interface mode is observed. As presented in spectrum 12, one can see that besides the features belonging to the Γ and K states of $WSe_2$, an additional state at $-2.0 \pm 0.03$ eV shows up in the $(\partial I/\partial V)_I$, representing the formation of a one-dimensional (1D) interface mode arising from the W–S bonds at the interface (illustrated by the $\kappa$ mapping in Supplementary Section 7). We note that a 1D interface state has also recently been observed at the hexagonal boron nitride–graphene interface[35].

The behaviour of the electronic structure of the conduction band across the interface is more straightforward. The conduction band minimum (CBM) is present as a pronounced peak in the $(\partial I/\partial V)_I$ spectrum for both $WSe_2$ and $MoS_2$, and is located at $1.0 \pm 0.03$ V for $WSe_2$ and at $0.45 \pm 0.03$ V for $MoS_2$. When approaching the interface, the CBM of $WSe_2$ shows downward band bending (Supplementary Section 8), whereas the CBM of $MoS_2$ shows upward band bending. Near the interface (spectra 8–10), the spectral features for the CBM are significantly damped, although the remains of individual components are still visible. The potential discontinuity is observed within a narrow interface region with a width of 1.0 nm (spectrum 9). Combining the mapping for both VBM and CBM, one can determine the quasiparticle band alignment across the $WSe_2$–$MoS_2$ interface as illustrated in Fig. 4e.

The conduction band offset (CBO) is determined to be 0.40 eV, with the CBM of $WSe_2$ above that of $MoS_2$. For unstrained $MoS_2$, the VBM is located $\sim 0.2 \pm 0.05$ eV above the Γ point, whereas this value is $0.65 \pm 0.05$ eV for unstrained $WSe_2$. Thus, without strain, the VBM of $WSe_2$ would have been $\sim 0.45 \pm 0.05$ eV above the VBM of $MoS_2$, which would have led to a type II alignment in the lateral heterojunction. However, the strain effect pushes the VBM of $MoS_2$ significantly above the Γ point, turning the band alignment into type I with a valence band offset (VBO) of approximately $-0.65 \pm 0.05$ eV.

## Conclusions

We used STM/STS to investigate the in-plane $WSe_2$–$MoS_2$ heterojunction formed with an atomically abrupt interface. The anisotropic strain induced by the lattice mismatch is mapped across the $MoS_2$ region with the help of the moiré pattern, which amplifies the minor atomic distortion and enables us to determine the full strain tensor. The strain in both the zigzag and armchair directions decrease with the distance from the interface but at strikingly different rates. We combine this strain mapping with mapping of the spatially varying electronic structure using constant $I$ spectroscopy to determine the deformation potential. We find that the anisotropic strain in the $MoS_2$ region narrows the quasiparticle bandgap with a ratio of $0.52 \pm 0.1$ eV per $\varepsilon_{aa}$%. In addition, the band offset (VBO of $0.65 \pm 0.05$ eV and CBO of $0.40 \pm 0.05$ eV) along with the 1D interface state are measured in this study. The lattice mismatch between the two components of the heterojunction converts the otherwise type II to type I band alignment through strain.

## Methods

Methods, including statements of data availability and any associated accession codes and references, are available at https://doi.org/10.1038/s41565-017-0022-x.

Received: 7 July 2017; Accepted: 2 November 2017;
Published online: 15 January 2018

## References

1. Mak, K. F., Lee, C., Hone, J., Shan, J. & Heinz, T. F. Atomically thin $MoS_2$: A new direct-gap semiconductor. *Phys. Rev. Lett.* **105**, 136805 (2010).
2. Splendiani, A. et al. Emerging photoluminescence in monolayer $MoS_2$. *Nano Lett.* **10**, 1271–1275 (2010).
3. Duan, X. D., Wang, C., Pan, A. L., Yu, R. Q. & Duan, X. F. Two-dimensional transition metal dichalcogenides as atomically thin semiconductors: opportunities and challenges. *Chem. Soc. Rev.* **44**, 8859–8876 (2015).
4. Liu, G. B., Xiao, D., Yao, Y. G., Xu, X. D. & Yao, W. Electronic structures and theoretical modelling of two-dimensional group-VIB transition metal dichalcogenides. *Chem. Soc. Rev.* **44**, 2643–2663 (2015).
5. Mak, K. F. & Shan, J. Photonics and optoelectronics of 2D semiconductor transition metal dichalcogenides. *Nat. Photon.* **10**, 216–226 (2016).
6. Fang, H. et al. Strong interlayer coupling in van der Waals heterostructures built from single-layer chalcogenides. *Proc. Natl Acad. Sci. USA* **111**, 6198–6202 (2014).
7. Tongay, S. et al. Tuning interlayer coupling in large-area heterostructures with CVD-grown $MoS_2$ and $WS_2$ monolayers. *Nano Lett.* **14**, 3185–3190 (2014).
8. Hong, X. et al. Ultrafast charge transfer in atomically thin $MoS_2$/$WS_2$ heterostructures. *Nat. Nanotech.* **9**, 682–686 (2014).
9. Chiu, M.-H. et al. Determination of band alignment in the single-layer $MoS_2$/$WSe_2$ heterojunction. *Nat. Commun.* **6**, 7666 (2015).
10. Wilson, N. R. et al. Determination of band offsets, hybridization, and exciton binding in 2D semiconductor heterostructures. *Sci. Adv.* **3**, e1601832 (2017).
11. Huang, C. et al. Lateral heterojunctions within monolayer $MoSe_2$–$WSe_2$ semiconductors. *Nat. Mater.* **13**, 1096–1101 (2014).
12. Gong, Y. J. et al. Vertical and in-plane heterostructures from $WS_2$/$MoS_2$ monolayers. *Nat. Mater.* **13**, 1135–1142 (2014).
13. Duan, X. et al. Lateral epitaxial growth of two-dimensional layered semiconductor heterojunctions. *Nat. Nanotech.* **9**, 1024–1030 (2014).
14. Li, M.-Y. et al. Epitaxial growth of a monolayer $WSe_2$-$MoS_2$ lateral p-n junction with an atomically sharp interface. *Science* **349**, 524–528 (2015).
15. Yun, W. S., Han, S. W., Hong, S. C., Kim, I. G. & Lee, J. D. Thickness and strain effects on electronic structures of transition metal dichalcogenides: 2H-$MX_2$ semiconductors (M=Mo, W; X=S, Se, Te). *Phys. Rev. B* **85**, 033305 (2012).
16. Johari, P. & Shenoy, V. B. Tuning the electronic properties of semiconducting transitionmetal dichalcogenides by applying mechanical strains. *ACS Nano* **6**, 5449–5456 (2012).
17. Li, H. et al. Optoelectronic crystal of artificial atoms in strain-textured molybdenum disulphide. *Nat. Commun.* **6**, 7381 (2015).
18. Shi, H., Pan, H., Zhang, Y. W. & Yakobson, B. I. Quasiparticle band structures and optical properties of strained monolayer $MoS_2$ and $WS_2$. *Phys. Rev. B* **87**, 155304 (2013).
19. Liu, Z. et al. Strain and structure heterogeneity in $MoS_2$ atomic layers grown by chemical vapour deposition. *Nat. Commun.* **5**, 5246 (2014).
20. Hui, Y. Y. et al. Exceptional tunability of band energy in a compressively strained trilayer $MoS_2$ sheet. *ACS Nano* **7**, 7126–7131 (2013).
21. Feng, J., Qian, X., Huang, C.-W. & Li, J. Strain-engineered artificial atom as a broad-spectrum solar energy funnel. *Nat. Photon.* **6**, 866–872 (2012).
22. He, K., Poole, C., Mak, K. F. & Shan, J. Experimental demonstration of continuous electronic structure tuning via strain in atomically thin $MoS_2$. *Nano Lett.* **13**, 2931–2936 (2013).

23. Zhu, C. R. et al. Strain tuning of optical emission energy and polarization in monolayer and bilayer $MoS_2$. *Phys. Rev. B* **88**, 121301 (2013).
24. Rice, C. et al. Raman-scattering measurements and first-principles calculations of strain-induced phonon shifts in monolayer $MoS_2$. *Phys. Rev. B* **87**, 081307 (2013).
25. Castellanos-Gomez, A. et al. Local strain engineering in atomically thin $MoS_2$. *Nano Lett.* **13**, 5361–5366 (2013).
26. Conley, H. J. et al. Bandgap engineering of strained monolayer and bilayer $MoS_2$. *Nano Lett.* **13**, 3626–3630 (2013).
27. Liu, N., Tersoff, J., Baklenov, O., Holmes, A. L. & Shih, C. K. Nonuniform composition profile in $In_{0.5}Ga_{0.5}As$ alloy quantum dots. *Phys. Rev. Lett.* **84**, 334–337 (2000).
28. Cosma, D. A., Wallbank, J. R., Cheianov, V. & Fal'ko, V. I. Moiré pattern as a magnifying glass for strain and dislocations in van der Waals heterostructures. *Faraday Discuss.* **173**, 137–143 (2014).
29. Jiang, Y. et al. Visualizing strain-induced pseudomagnetic fields in graphene through an hBN magnifying glass. *Nano Lett.* **17**, 2839–2843 (2017).
30. Zhang, C. et al. Interlayer couplings, Moiré patterns, and 2D electronic superlattices in $MoS_2/WSe_2$ hetero-bilayers. *Sci. Adv.* **3**, e1601459 (2017).
31. Goodier, J. N. Concentration of stress around spherical and cylindrical inclusions and flaws. *J. Appl. Mech. Trans. ASME* **55**, 39–44 (1933).
32. Kang, J., Tongay, S., Zhou, J., Li, J. & Wu, J. Band offsets and heterostructures of two-dimensional semiconductors. *Appl. Phys. Lett.* **102**, 012111 (2013).
33. Guzman, D. M. & Strachan, A. Role of strain on electronic and mechanical response of semiconducting transition-metal dichalcogenide monolayers: An ab-initio study. *J. Appl. Phys.* **115**, 243701 (2014).
34. Zhang, C. et al. Probing critical point energies of transition metal dichalcogenides: surprising indirect gap of single layer $WSe_2$. *Nano Lett.* **15**, 6494–6500 (2015).
35. Park, J. et al. Spatially resolved one-dimensional boundary states in graphene–hexagonal boron nitride planar heterostructures. *Nat. Commun.* **5**, 5403 (2014).


## Acknowledgements

This research was supported with grants from the Welch Foundation (F-1672), the US National Science Foundation (NSF) (DMR-1306878, EFMA-1542747) and the Materials Research Science and Engineering Center (DMR-1720595). L.J.L. acknowledges support from KAUST (Saudi Arabia), MOST and TCECM, Academia Sinica (Taiwan) and AOARD FA23861510001 (USA). C.Z acknowledges support from the National Natural Science Foundation of China (Grant No. 11774268). Y.S.S acknowledges support from the Yan Jici Talent Students Program. This work made use of the electron microscopy facility of the Cornell Center for Materials Research with support from the NSF (DMR-1719875 and DMR-1429155).

## Author contributions

C.Z. carried out the STM/S measurements. M.-Y.L. and L.-J.L. performed the chemical vapour deposition growth of $WSe_2$–$MoS_2$ heterojunctions. Y.S. helped determine strain tensors from distorted moiré patterns. Y.H. and D.A.M. performed the scanning transmission electron microscopy investigations. J.T. identified the mechanisms of strain relaxation and explained the strain distribution. C.-K.S. advised on the experiments and provided input on the data analysis. C.-K.S. and C.Z. wrote the paper with input from the co-authors.

## Competing interests

The authors declare no competing financial interests.

## Additional information

**Supplementary information** is available for this paper at https://doi.org/10.1038/s41565-017-0022-x.

**Reprints and permissions information** is available at www.nature.com/reprints.

**Correspondence and requests for materials** should be addressed to C.Z. or C.-K.S.

## Methods

**Growth of the lateral $WSe_2$–$MoS_2$ heterojunction.** The $WSe_2$–$MoS_2$ lateral heterojunction was grown using the developed two-step chemical vapour deposition method[14]. First, a monolayer $WSe_2$ single crystal was grown on the HOPG substrate. The $WO_3$ powder (0.6 g) was placed in a quartz boat placed in the heating zone centre of the furnace, and the HOPG substrate was placed at the downstream side. The Se powder was placed in a separate quartz boat at the upstream side of the furnace. An Ar/$H_2$ flow (Ar = 90 sccm, $H_2$ = 6 sccm) was used, and the chamber pressure was controlled at 20 torr. The centre heating zone and Se were heated to 935 °C and 260 °C for growth, respectively. After reaching the desired growth temperature, the heating zone was held at that temperature for 15 min and the furnace was then naturally cooled down to room temperature. The $WSe_2$ sample was then placed into a separate furnace for the second step of $MoS_2$ growth. The setup for $MoS_2$ synthesis was similar to that for $WSe_2$, except the sources were switched to $MoO_3$ (0.6 g) and S. The Ar gas flow was set at 70 sccm and the pressure was controlled at 40 torr. The $WSe_2$ sample was placed downstream of the $MoO_3$ boat. The centre zone and S were heated to 755 °C and 190 °C, respectively and held for 15 min for synthesis, and then naturally cooled down to room temperature.

**Scanning tunnelling microscopy and spectroscopy.** All STM investigations reported here were acquired at 77 K in ultrahigh vacuum (UHV; base pressure $< 6 \times 10^{-11}$ torr). Electrochemically etched W-tips were cleaned in situ with electron beam bombardment. Tunnelling bias was applied to the sample.

The $(\partial I/\partial V)_I$ spectra were taken at a constant tunnelling current (with feedback loop on) using a lock-in amplifier with a modulation voltage of 10 mV and at a frequency of 914 Hz. Meanwhile, the tip-to-sample separation $Z$ changes corresponded to the scanning bias $V$ to maintain the constant current. Thus, $(\partial I/\partial V)_I - V$ and $Z - V$ were acquired simultaneously. The d$I$/d$V$ spectroscopy at constant $Z$ were taken using similar parameters to those of the lock-in amplifier (10 mV at a frequency of 914 Hz) but with the feedback loop off. The tunnelling decay constant $\kappa$ is equal to $-d\ \ln I/2dz \equiv -(dI/dz)/2I_0$. The $dI/dZ$ can be acquired using the lock-in amplifier to apply a $Z$-modulation with an amplitude of 0.01 nm. The frequency of the $Z$-modulation (914 Hz) is faster than the feedback time constant. If the sample bias is swept slowly with the feedback loop on, the $(\partial I/\partial Z)_I - V$ (that is, $\kappa - V$) can be acquired.

**Annular dark-field scanning transmission electron microscopy.** ADF-STEM imaging was conducted using a FEI TITAN operated at 120 kV with a ~15 pA probe current. The acquisition time per pixel was less than 8 ms, but multiple images (10–20) were acquired and cross-correlated afterwards to improve the signal-to-noise ratio and to reduce the scan noise introduced by sample drift. A 30 mrad convergence angle and a 40 mrad inner collection angle were used, the contrast of which is proportional to $Z^\gamma$, where $Z$ is the atomic number and $1.3 < \gamma < 2$.

**Data availability.** The datasets generated and/or analysed during the current study are available from the corresponding authors on reasonable request.